frontiers | Frontiers in Built Environment

TYPE Original Research
PUBLISHED 18 September 2025
DOI 10.3389/fbuil.2025.1672953

OPEN ACCESS

EDITED BY
Shiyu Zhuang,
Tsinghua University, China

REVIEWED BY
Amir Ali Shahmansouri,
Washington State University, United States
Yan Sun,
Wuhan University of Technology, China

*CORRESPONDENCE
Xuli Li,
lixuli@whpu.edu.cn
Shefeng Li,
lishengfeng@whpu.edu.cn

RECEIVED 25 July 2025
ACCEPTED 25 August 2025
PUBLISHED 18 September 2025

CITATION
Li X, Zhang J, Zhang Y, Ding S, Nie M and Li S (2025) Preparation of iron tailings-based cementitious materials based on mechanochemical reinforcement. *Front. Built Environ.* 11:1672953. doi: 10.3389/fbuil.2025.1672953

Preparation of iron tailings-based cementitious materials based on mechanochemical reinforcement

Xuli Li[1]*, Jinhui Zhang[2], Yong Zhang[1], Siyu Ding[1], Miaomiao Nie[1] and Shefeng Li[1]*

[1]Hubei Province Key Laboratory of Agricultural Waste Resource Utilization, School of Chemistry and Environmental Engineering, Wuhan Polytechnic University, Wuhan, China, [2]College of Chemical Engineering, Fuzhou University, Fuzhou, China

The large-scale stacking of iron tailings poses challenges to the eco-environment and mining industry. Materializing tailings treatment is an effective way to solve this bulk solid waste problem. In this study, using iron tailings rich in hematite and calcite as the main raw material, we prepared a cementitious material with about 80wt% iron tailings content by mechanical ball milling and alkali activation, with the addition of cement and slag powder. Elemental analysis of the raw materials revealed Fe, Ca, and Si contents in the iron tailings of 41.248%, 33.949%, and 20.211%, respectively, and the main mineral phases were calcite, hematite, and quartz. Our research demonstrated that mortar made from iron tailings ball-milled for 15 min exhibited the best properties, with an activity index of 108.1%. When the alkali activator content was 6%, the compressive strength of the test blocks was optimal, reaching 7.9 MPa after 28-day curing. We also conducted tests on standard consistency, setting time, and hydraulic properties, confirming the potential activity of iron tailings. Using orthogonal experiments, we optimized the proportions of each component and explored the effects of tailings content and water - binder ratio on the mechanical properties of the samples. Furthermore, we analyzed the microstructure of the cementitious material with different tailings contents and curing ages using FTIR and XRD and proposed its hydration mechanism.

KEYWORDS

iron tailings, cementitious materials, alkali excitation, mechanical activation, ball milling

1 Introduction

The disposal and comprehensive utilization of metal tailings represent a critical strategic imperative for ensuring China's resource security (Lan et al., 2021a), ecological safety, and sustainable development. As mineral resources underpin national economic growth and strategic stability, the massive accumulation of tailings (exceeding 60 billion tons in China by 2020) poses severe challenges (Yu et al., 2024; Zhao et al., 2023). For instance, iron tailings storage not only occupies vast land resources but also harbors

environmental risks such as dam failures and heavy metal contamination (Yan et al., 2024). Additional threats include airborne particulate emissions and chemical leaching, which jeopardize ecosystems and public health. In response, China has strengthened regulatory frameworks through policies like the *Management Measures for Tailings Pollution Prevention and Control* (Sun et al., 2025), mandating prioritized recycling of tailing water and promoting tailings as substitutes for construction raw materials under its *Carbon Peaking Action Plan* (Wei et al., 2023; Xiang et al., 2024a; Xiang et al., 2023). These efforts aim to address the intertwined challenges of safe disposal, pollution mitigation, and resource recovery (Lan et al., 2020b; Wei et al., 2024). Current research prioritizes the efficient utilization of iron tailings through approaches such as recovery of valuable components, development of green building materials, mine goaf remediation, and synthesis of functional materials (Lan et al., 2021b; Wang et al., 2024). Technological advancements in these areas hold strategic significance for reducing reliance on virgin resources, minimizing environmental footprints, and advancing the green transformation of the mining industry (Sun et al., 2021b).

The comprehensive utilization of iron tailings has achieved significant progress in recent years, spanning four key domains: resource recovery, high-value product development, environmental remediation, and construction material applications (Almeida et al., 2023; Liu et al., 2023; Pan et al., 2025a). In resource recovery, valuable metals such as molybdenum, zinc, titanium, and copper are efficiently extracted through processes like flotation and magnetic separation (Lan et al., 2021e; Sadeghieh et al., 2020). For high-value utilization, iron tailings are engineered into advanced materials, including ceramic granules with compressive strengths up to 56.5 MPa, nano-magnetic cellulose for heavy metal adsorption (Lan et al., 2019a; Närhi et al., 2012), and $FeSi_2$-glass ceramic composites (Tian et al., 2024; Xiang et al., 2024b). Environmental applications involve transforming iron tailings into silicon slow-release fertilizers or soil amendments via mechanical grinding, acidification, or organic modification, which enhance soil fertility and crop yields in saline-alkali conditions (Pan et al., 2024a; Que et al., 2024). In construction, modified iron tailings improve road durability, hydrophobic concrete performance (Jahanshahi and Ghanizadeh, 2024; Lan et al., 2019b), and unconfined compressive strength of stabilized soils (Cui et al., 2025; Qiu et al., 2024). To address inherent low reactivity, activation strategies such as mechanical grinding (optimizing particle size and surface area), chemical alkali activation (using NaOH or Na_2SiO_3 to stimulate cementitious reactions) (Lan et al., 2021d; Li et al., 2025), thermal treatment (650 °C–700 °C calcination to generate amorphous phases), and hybrid approaches (e.g., thermo-mechanical coupling) have been developed (Pramanik et al., 2024; Qin et al., 2024). Notably, synergistic activation elevates copper tailings' activity from 5.6% to 89.91%, enabling their large-scale use in cementitious materials (Chen et al., 2025; Gong et al., 2021; Pan et al., 2024b). These advancements not only promote the resource efficiency and value-added recycling of iron tailings but also provide critical technological pathways for mitigating environmental impacts and advancing sustainable mining practices (Pan et al., 2025b; Zeng et al., 2025; Zhang et al., 2025b).

FIGURE 1
Photograph of iron tailings.

This study systematically investigates the synthesis and optimization of cementitious materials derived from copper-iron tailings through a mechanochemical activation approach. The research framework encompasses four key phases: (1) Characterization of tailings' particle size distribution and specific surface area under varying ball milling durations to identify optimal activation parameters and elucidate mechanochemical mechanisms; (2) Evaluation of compressive strength development under different alkali activator dosages and curing periods to establish optimal mechanical-chemical activation conditions; (3) Formulation optimization via orthogonal experiments incorporating slag powder, cement, NaOH, and Na_2SiO_3 to determine the ideal component ratios for performance enhancement; (4) Microstructural evolution analysis and hydration mechanism exploration through water-to-binder ratio adjustments and multi-scale characterization at optimized tailings incorporation levels. This integrated methodology combines process parameter optimization, multi-factor performance testing, and mechanistic investigation to achieve sustainable valorization of copper-iron tailings in cementitious material applications.

2 Materials and methods

2.1 Materials

2.1.1 Iron tailings

The iron tailings used in this experiment (Figure 1) were formed by the accumulation of solid waste generated after magnetic separation and flotation processes to extract copper and iron concentrates.

Chemical composition of iron tailings: XRF analysis results are shown in Table 1 below:

As evidenced by Table 1, iron (Fe) constitutes the most abundant element in the tailings, representing 41.248% of the total composition. The distinct reddish coloration of the tailings strongly indicates the presence of considerable hematite (Fe_2O_3) content. Calcium (Ca) follows as the second most prevalent element at 33.949%, accompanied by silicon (Si) at 20.211%. This elemental distribution suggests the existence of substantial calcium silicate compounds within the tailings. The remaining elements are present in relatively minor concentrations.

TABLE 1 Chemical composition of copper-iron tailings (wt%).

Composition	Fe	Ca	Si	K	Mn	Sr	Cu	S	Other
Content/%	41.248	33.949	20.211	1.204	0.948	0.913	0.591	0.584	0.352

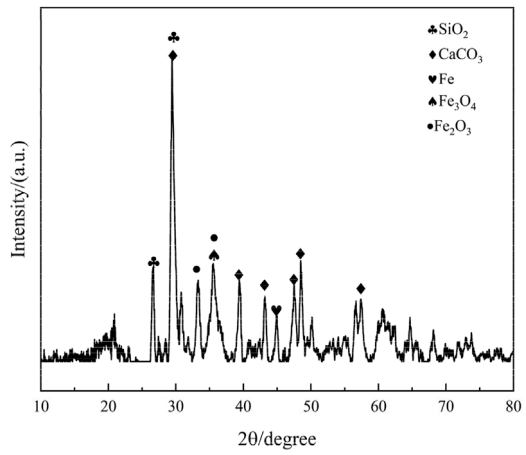

FIGURE 2
XRD pattern of copper and iron tailings.

Phase composition and crystal structure of copper-iron tailings: XRD analysis results are presented in the following Figure 2.

The XRD pattern of the iron tailings reveals that the primary mineral constituent in the experimental tailings is calcite ($CaCO_3$), which is consistent with the high calcium content identified in the XRF analysis. Additionally, the sample contains significant quantities of quartz (SiO_2), hematite (Fe_2O_3), and magnetite (Fe_3O_4), indicating a complex mineralogical composition. The presence of quartz suggests a siliceous component, while hematite and magnetite are indicative of the iron-rich nature of the tailings. These findings align with the particle size distribution and chemical composition data, further confirming the heterogeneous nature of the iron tailings. The coexistence of these minerals not only influences the reactivity of the tailings during mechanical and chemical activation but also plays a critical role in the hydration process and the formation of cementitious products. This mineralogical composition provides a solid foundation for understanding the behavior of the tailings in subsequent experiments and their potential for resource utilization in cementitious materials.

The FTIR spectrum of the iron tailings, as illustrated in Figure 3, provides detailed insights into the functional groups and chemical bonds present in the sample. Characteristic absorption peaks at 3,352 cm^{-1} and 2,513 cm^{-1} are attributed to the asymmetric stretching vibrations of -OH groups in water molecules, indicating the presence of adsorbed or structural water within the tailings. The distinct peaks observed at 1,013 cm^{-1}, 872 cm^{-1}, and 711 cm^{-1} are associated with Si-O stretching vibrations. Specifically, the peak at 1,013 cm^{-1} arises from asymmetric Si-O stretching, while the peaks at 872 cm^{-1} and 711 cm^{-1} result from symmetric Si-O stretching, confirming the presence of quartz (SiO_2) in the iron tailings. Furthermore, the intense absorption peak at 1,436 cm^{-1} is characteristic of C-O stretching vibrations, which strongly suggests a substantial carbonate content in the tailings, likely originating from calcite ($CaCO_3$). Additionally, a sharp vibrational peak at 3,691 cm^{-1}, corresponding to bound water, which is caused by hydration reactions, resulting in an increase in wavenumber, further supporting the mineralogical composition identified by XRD analysis. These FTIR findings collectively corroborate the presence of quartz, carbonates, and calcium-containing phases in the iron tailings, providing a comprehensive understanding of their chemical and structural properties.

Further investigation into the particle size distribution and equivalent diameter of the iron tailings is presented in Table 2 and Figure 4. The particle size distribution curve exhibits a normal distribution pattern, with the majority of particles ranging between 1 and 100 μm, which is consistent with the mineralogical composition and reactivity requirements for cementitious applications. The characteristic diameters D_{10}, D_{50}, and D_{90}, which represent the particle sizes at 10%, 50%, and 90% cumulative distribution, are determined to be 1.858 μm, 17.307 μm, and 81.413 μm, respectively. These values highlight the fine-grained nature of the tailings, with a significant proportion of particles falling within the micron range. Additionally, the particle size dispersion index, a key parameter reflecting the uniformity of particle distribution, is calculated to be 4.6 for these iron tailings. This relatively high dispersion index indicates a broad particle size distribution, which may influence the packing density, reactivity, and overall performance of the tailings in cementitious systems. The combination of fine particle sizes and a wide distribution range suggests that the iron tailings possess a heterogeneous microstructure, which could contribute to both challenges and opportunities in their utilization as a supplementary material in construction applications. These findings provide valuable insights into the physical characteristics of the tailings, which are critical for optimizing their processing and application in sustainable building materials.

2.1.2 Cement

The cement used in the experiments was commercially available P.O42.5 cement with the following composition:

As evidenced by Table 3 and Figure 5, calcium (Ca) constitutes the predominant elemental component in the cement, accounting for 76.249% of the total composition, which underscores its critical role in the formation of calcium silicate hydrates (C-S-H) and other cementitious phases during hydration. This is followed by silicon (Si) and iron (Fe) at 11.198% and 7.286%, respectively, which contribute to the structural integrity and mechanical properties of the cement matrix. Trace elements, including sulfur (S), potassium (K), and strontium (Sr), are also detected, albeit in minor quantities, suggesting their potential influence on the chemical reactivity and durability of the cement.

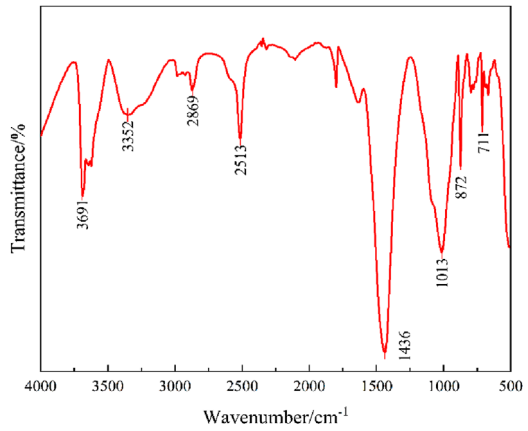

FIGURE 3
FTIR analysis profile of iron tailings.

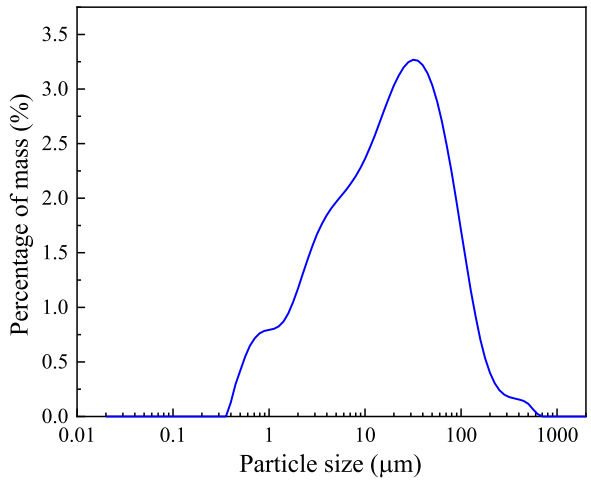

FIGURE 4
Copper and iron tailings particle size distribution chart.

TABLE 2 Equivalent particle size table of iron tailings (μm).

	D_{10}	D_{50}	D_{90}
particle size (μm)	1.858	17.307	81.413

The phase composition analysis, as depicted in Figure 5, reveals calcite ($CaCO_3$) as the primary crystalline phase, which aligns with the high calcium content identified in the elemental analysis. Quartz (SiO_2) is identified as the secondary phase, consistent with the silicon content, and contributes to the overall strength and stability of the cement. Additionally, minor constituents, including hematite (Fe_2O_3) and other unidentified phases, are detected within the cement matrix. These phases, though present in smaller amounts, may play a role in the coloration, density, and long-term performance of the cement. The coexistence of these phases highlights the complex and heterogeneous nature of cement, which is essential for understanding its hydration behavior and optimizing its application in construction materials. These findings provide a comprehensive foundation for further exploration of the cement's properties and its potential for sustainable utilization in engineering applications.

2.1.3 Slag powder

The slag powder used in the experiment was commercially available S95 grade slag powder with the following composition:

As shown in Table 4, calcium (Ca) is the predominant element in the slag powder, followed by silicon (Si) and aluminum (Al), suggesting the presence of substantial $CaCO_3$, SiO_2, and Al_2O_3 components. The XRD pattern in Figure 6 exhibits a broad "hump" between 15 ° and 25 ° without distinct characteristic peaks, indicating a highly amorphous structure with minimal crystalline ordering. This structural characteristic implies significant potential reactivity of the slag powder. Under alkaline conditions, the activation of SiO_2 and Al_2O_3 can promote hydration reactions, generating cementitious compounds that enhance the binding properties of cementitious materials.

2.1.4 Alkali activators

The alkaline activator used in this experiment was prepared from liquid sodium silicate and NaOH powder. The sodium silicate, purchased from Tianjin Zhonglian Chemical Reagent Co., Ltd., has a SiO_2 content of 35%, a Baume degree of 40, and a modulus of 3.3. The NaOH, commercially available as analytical grade reagent, has a purity exceeding 96%.

2.2 Methods

The experimental procedure commenced with mechanical ball milling of iron tailings. The copper-iron tailings were initially fragmented into small pieces and dried at 80 °C for 12 h to achieve a moisture content below 1%. The dried tailings were then subjected to planetary ball milling at 200 rpm for varying durations. Subsequently, the milled tailings were blended with appropriate proportions of cement and slag powder in a mortar mixer for 2 min. A pre-prepared alkaline activator solution was introduced, followed by the addition of distilled water at the designated water-to-binder ratio, with further mixing for 2 min. The mixture was then manually homogenized and poured into 40 × 40 × 160 mm triple-gang molds pre-coated with mineral oil. Compaction was achieved using a vibration table for 2 min. The specimens were cured in a standard constant temperature and humidity chamber (20 °C, 95% RH) for 24 h before demolding, followed by continued curing under identical conditions until reaching the specified testing ages.

In this study, multiple factors influence the performance of the cementitious materials. While investigating each factor at various levels through controlled variable experiments would be prohibitively labor-intensive, orthogonal experimental design offers an efficient alternative by selecting representative combinations from all possible permutations. This approach significantly reduces resource expenditure while enabling rapid and reliable optimization. Under optimal mechanical-chemical activation conditions, the effects of varying contents of iron tailings, cement, slag powder, sodium hydroxide, and sodium silicate on the performance of

TABLE 3 Chemical elemental composition of cement (wt%).

Composition	Ca	Si	Fe	S	K	Sr	Ti	Zn	Other
Content/%	76.249	11.198	7.286	1.511	1.418	0.975	0.353	0.244	0.766

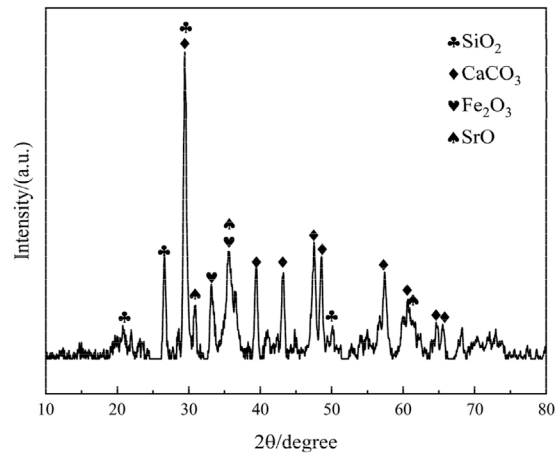

FIGURE 5
XRD pattern of cement.

cementitious materials were systematically investigated. A three-level orthogonal array with nine experimental groups was employed to evaluate the influence of each component and determine the optimal composition ratio. After the specimens were cured to the corresponding age, they were removed and soaked in anhydrous ethanol for 72 h to terminate the hydration reaction, and then the specimens were dried in an oven (60 °C) for 24 h and removed for subsequent microscopic characterization tests (Table 5).

The selected proportions (30 g slag, 52 g cement, 16 g NaOH, 8 g sodium silicate per 100 g tailings) were primarily designed to achieve optimal geopolymerization conditions based on fundamental alkali-activated material chemistry. The slag content (30 g) provides sufficient Ca^{2+}/Al^{3+} for C-A-S-H gel formation while maintaining a target Ca/Si ratio ≈1.1. Cement (52 g) ensures critical pH > 13 via $Ca(OH)_2$ generation and acts as nucleation sites. NaOH (16 g) delivers excess alkali (Na_2O = 41% of slag mass) to overcome tailings acidity and sustain $[Na^+]$ >3 mol/L for dissolution kinetics. Sodium silicate (8 g, modulus = 2.0) balances Si/Al = 2.5 and modulates reaction pathways with NaOH. These ratios align with established geopolymer thermodynamic frameworks targeting network-forming Si-O-Al bonds, though no specific hydration model was explicitly cited. The formulation holistically addresses stoichiometric (Ca/Si, Na/Si), kinetic (alkali concentration), and structural (Si/Al) requirements for effective activation.

2.3 Characterizations

The experimental setup comprised specialized equipment including a JJ-5 cement mortar mixer (Shangyu Yueda Instrument Co.), DYE-300 universal testing machine (Hebei Jingrui Keyu), Malvern Mastersizer 2000 laser particle analyzer (Malvern Panalytical, United Kingdom), Rigaku Smart Lab SE X-ray diffractometer (Cu Kα radiation, 2 °/min scan rate, 10 °–80 ° range), and Thermo Scientific Nicolet 6700 FTIR spectrometer. Characterization techniques were conducted as follows: X-ray fluorescence spectroscopy (EDX-7000, Shimadzu, Na–U detection range, Rh target, 4–50 kV) quantified elemental composition, while particle size distribution was analyzed via wet dispersion with 5 min ultrasonication. Compressive strength tests (GB/T 17671-1999) employed a loading rate of 2.4 kN/s, calculated as $P = F/A$, where F (kN) denotes failure load and A (mm^2) the bearing area. Reactivity indices were evaluated per GB/T 12957-2005 by substituting 30% cement with tailings, curing samples for 28 days, and calculating $k = R1/R2$, where $R1$ and $R2$ represent compressive strengths of blended and pure cement mortars, respectively. Latent hydraulic activity was assessed through 8:2 or 9:1 tailings-gypsum mixtures molded into test cakes, cured at 20 °C/95% RH for 7 days, followed by 3-day water immersion to evaluate structural integri.

3 Results and discussion

3.1 Effect of mechanical ball milling on the properties of iron tailings

3.1.1 Effect of mechanical ball milling on particle size of iron tailings

With the prolongation of ball milling time, the iron tailings will gradually refine and tend to be spherical, and the particle size will gradually decrease. The cumulative distribution curves of the particle size of copper and iron tailings under different ball milling times (0, 10, 15, 20, 25 and 30 min) determined by Malvern laser particle size analyzer are as follows:

The results demonstrate that under mechanical action, the raw iron tailings undergo progressive fragmentation through energy transfer from the grinding media, leading to reduced particle size and increased specific surface area. The particles gradually attain a more spherical morphology with improved size distribution uniformity. As shown in Figure 7, the particle size distribution curves exhibit a distinct shift toward finer sizes with prolonged milling duration, transitioning from a broad to a narrow distribution profile.

As presented in Table 6, the initial median particle size (D_{50}) of 17.307 μm progressively decreased to 11.475, 10.658, 9.193, 8.891, and 6.447 μm after 10, 15, 20, 25, and 30 min of ball milling, respectively. Over the 0–30-min milling period, D_{50} was reduced from 11.475 μm to 6.447 μm. Similarly, D_{10}

TABLE 4 Chemical elemental composition of slag powder (wt%).

Composition	Ca	Si	Al	Ti	Sr	Zr	Fe	Mn	Other
Content/%	67.021	16.284	8.046	1.750	1.568	1.198	1.125	0.925	2.083

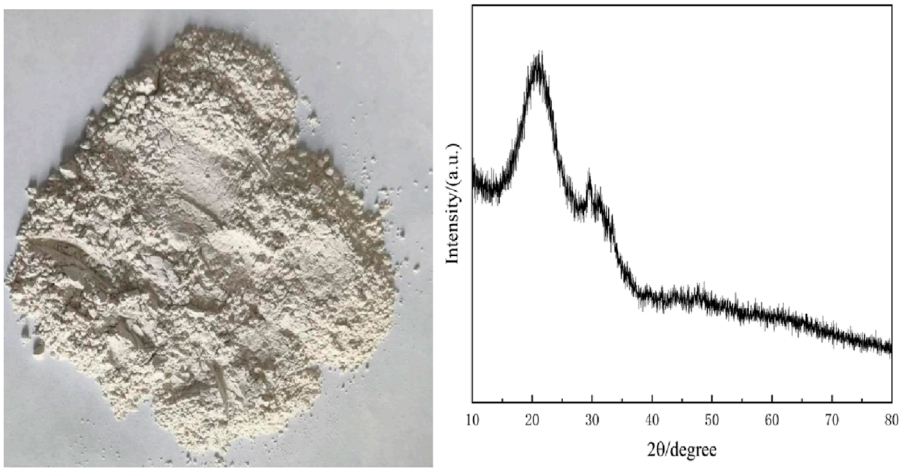

FIGURE 6
Appearance morphology and XRD spectrum of slag powder.

TABLE 5 Table of factors and levels for L9(34) orthogonal test.

Levels	Factors			
	Slag powder/g	Cement/g	NaOH/g	Sodium silicate/g
	A	B	C	D
1	10	36	8	8
2	20	44	16	16
3	30	52	24	24

decreased from 1.858 μm to 1.033 μm, while D_{90} showed a significant reduction from 81.413 μm to 26.853 μm. Concurrently, the specific surface area increased from 1.21 m^2/g to 2.07 m^2/g, confirming progressive particle refinement throughout the milling process. However, milling efficiency exhibited a gradual decline with prolonged duration, accompanied by increased material loss due to adhesion on the mill walls and grinding media surfaces, particularly beyond 15 min. This is considered to be caused by the "aggregation" phenomenon of the powder. At the same time, this will also lead to a certain decrease in the specific surface area of the material. For example, the specific surface area at 25 min has slightly decreased. This phenomenon resulted in substantial mechanical energy dissipation and operational inefficiency. Therefore, considering the balance between particle refinement and energy consumption, an optimal milling duration of 15 min was determined for subsequent parametric studies.

3.1.2 Changes in chemical bonding of iron tailings before and after ball milling

The median particle sizes at 10, 15, 20, and 25 min of ball milling showed minimal variation, with no significant changes in particle size distribution or FTIR spectra. Consequently, only the 20-min milled tailings and raw tailings were selected for comparative FTIR analysis.

As shown in Figures 2, 8, the iron tailings exhibited similar spectral profiles before and after milling. A sharp vibrational peak at 3,691 cm^{-1}, corresponding to $CaCO_3$ in the tailings, demonstrated reduced intensity post-milling. Absorption peaks at 3,382 cm^{-1}, 2,512 cm^{-1}, and 1794 cm^{-1} were attributed to -OH stretching vibrations in hydrated minerals. The peak at 1,449 cm^{-1}, associated with O-C-O stretching vibrations, originated from carbonate species, while the peaks near 1,094 cm^{-1}, 869 cm^{-1}, and 711 cm^{-1} were assigned to Si-O-Si stretching vibrations. Following ball milling, the initially sharp peaks at 1,449 cm^{-1} and 1,094 cm^{-1}

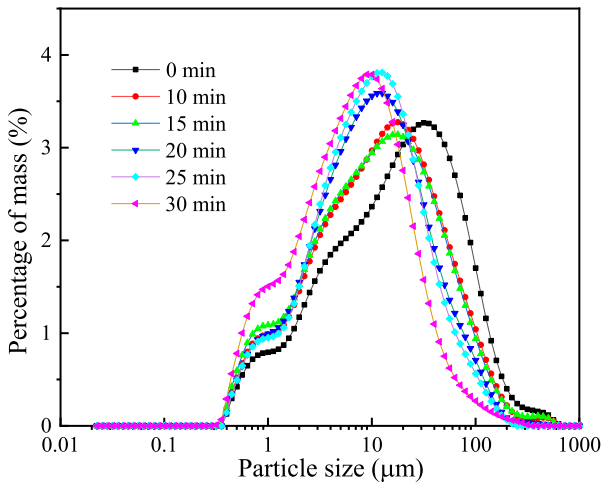

FIGURE 7
Cumulative curve of particle size distribution of iron tailings under different ball milling time.

broadened significantly, indicating the disruption of Si-O and C-O bonds. This structural alteration led to the degradation of crystalline integrity and a transition toward an amorphous state.

3.1.3 Activation index change of iron tailing reaction after ball milling

Using cement mortar cured for 28 days as the reference sample, the reactivity of mortar specimens incorporating 30% iron tailings was evaluated (Table 7).

As shown in Figure 9, the compressive strength of the mortar exhibited a progressive increase with milling duration, reaching its maximum enhancement at 15 min. At 3 days of curing, the compressive strength of the mortar prepared with raw, unmilled tailings was measured at 7.3 MPa, while the specimen milled for 15 min demonstrated a significant improvement, achieving a compressive strength of 10.2 MPa. However, extending the milling duration beyond 15 min resulted in a gradual decline in compressive strength, with the value decreasing from 10.2 MPa at 15 min to 8.0 MPa at 30 min. This trend suggests that excessive milling may lead to particle agglomeration or over-grinding, which could negatively impact the material's performance.

At the 28-day curing stage, the compressive strength showed a more pronounced improvement, increasing from 11.2 MPa at 10 min of milling to 21.3 MPa at 15 min, representing the most substantial enhancement in mechanical properties. This significant increase underscores the effectiveness of 15 min of mechanical ball milling in activating the iron tailings, optimizing their reactivity, and enhancing their contribution to the mortar's strength development.

Complementing these findings, Figure 10 illustrates the reactivity index of the tailings, which further supports the observed trends. The reactivity index of unmilled tailings was initially 42.6%, indicating limited activation. However, after 15 min of milling, the reactivity index peaked at 108.1%, demonstrating a remarkable improvement in the tailings' potential to participate in hydration reactions. Beyond this optimal milling duration, the reactivity index gradually decreased, aligning with the decline in compressive strength and reinforcing the conclusion that 15 min of milling represents the optimal balance between particle refinement and activation.

These results collectively highlight the critical role of mechanical ball milling in enhancing the reactivity and performance of iron tailings in cementitious systems. The findings provide valuable insights into the optimization of milling parameters for sustainable construction materials, emphasizing the importance of balancing milling duration to achieve maximum activation without compromising material properties.

3.2 Preparation of iron tailings-based cementitious materials

3.2.1 Effect of different factors on the strength of cementitious materials

The orthogonal experimental results revealed the influence of various factors on the strength of cementitious materials. As shown in Table 8 and Figure 11, at the 7-day curing stage, the range values for factors A (slag powder), B (cement), C (sodium hydroxide), and D (sodium silicate) were calculated as 1.53, 2.00, 0.57, and 0.97, respectively. The largest range value for factor B (cement) indicates its predominant influence on the compressive strength at 7 days, followed by factor A (slag powder), while factors C and D exhibited minimal effects. Thus, the order of influence on material performance was determined as B > A > D > C. At the 28-day curing stage, factor A (slag powder) demonstrated the highest range value of 3.1, emerging as the most influential factor, with factor B (cement) following closely. The revised order of influence was A > B > D > C. In Table 9, the K-values represent the average performance at each factor level, with higher K-values indicating better performance. The optimal combinations for 7-day and 28-day curing were identified as $B_3A_3D_2C_1$ and $A_3B_3D_2C_1$, respectively. Consequently, the addition of 30 g slag powder, 52 g cement, 16 g sodium hydroxide, and 8 g sodium silicate were determined to yield the optimal performance of the cementitious material.

3.2.2 Effect of different tailings dosage on compressive strength

As shown in Figure 12, the compressive strength of the cementitious materials exhibited a gradual decline with increasing iron tailings content, reflecting the influence of tailings incorporation on the material's mechanical performance. At a 50% tailings incorporation rate, the compressive strengths were measured at 5.9 MPa, 8.2 MPa, and 9.6 MPa for 3-day, 7-day, and 28-day curing periods, respectively. In contrast, when the tailings content was increased to 90%, these values decreased significantly to 1.4 MPa, 1.9 MPa, and 2.0 MPa for the same curing durations. This notable reduction in compressive strength is primarily attributed to the slow dissolution of calcite ($CaCO_3$), the predominant crystalline phase in the iron tailings, under alkaline conditions. Compared to other reactive components such as cement and slag, the tailings exhibit lower reactivity, contributing fewer active components to the hydration process and resulting in the formation of limited hydration products. Consequently, higher tailings content leads to

10.3389/fbuil.2025.1672953

TABLE 6 Equivalent particle size and specific surface area of iron tailings.

Ball milling time(min)	D_{10} (μm)	D_{50} (μm)	D_{90} (μm)	Specific surface area(m^2/g)
0	1.858	17.307	81.413	1.21
10	1.500	11.475	59.589	1.47
15	1.348	10.658	57.129	1.59
20	1.507	9.193	44.039	1.60
25	1.554	8.891	38.290	1.54
30	1.033	6.447	26.853	2.07

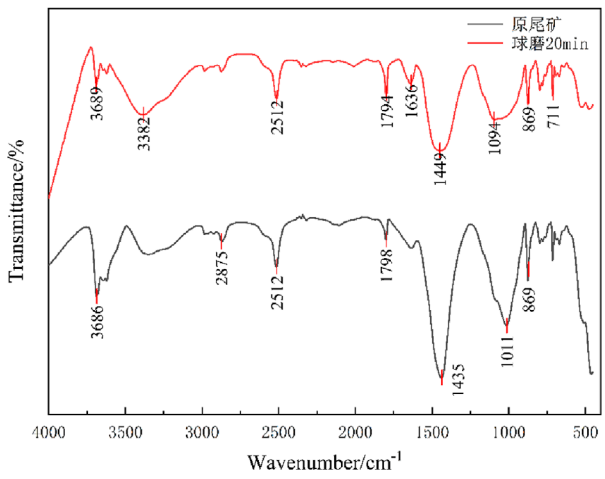

FIGURE 8
Infrared spectra of iron tailings before and after ball milling.

a reduction in the overall compressive strength of the cementitious materials.

The strength decline occurs in two distinct phases: a more gradual reduction is observed at tailings contents between 80% and 90%, while a rapid decrease is evident between 70% and 80% tailings incorporation. This behavior suggests a critical threshold in the tailings content beyond which the material's mechanical properties are significantly compromised. Despite the lower compressive strength observed in cementitious materials with high tailings content, these materials remain suitable for applications where high strength is not a critical requirement, such as in backfill materials, road base layers, or non-structural construction elements.

These findings highlight the trade-off between tailings utilization and mechanical performance, emphasizing the importance of optimizing tailings content based on the intended application. The results also underscore the potential for using iron tailings in sustainable construction materials, particularly in scenarios where moderate strength is acceptable, thereby contributing to the efficient utilization of industrial by-products and reducing environmental impact.

3.2.3 Effect of different water cement ratio on compressive strength

The water-to-binder ratio (w/b) is a critical factor influencing the compressive strength of cementitious materials. Using the optimal composition ratio determined from previous orthogonal experiments, four w/b levels (0.40, 0.45, 0.50, 0.55) were investigated to analyze their effects on compressive strength. As shown in Figure 13, the compressive strength of iron tailings-based cementitious materials decreased progressively with increasing w/b ratio. When the w/b ratio increased from 0.40 to 0.55, the 3-day, 7-day, and 28-day compressive strengths declined significantly from 3.5 MPa, 5.2 MPa, and 5.5–1.4 MPa, 1.9 MPa, and 2.4 MPa, respectively. This reduction is attributed to the adverse effects of excessive water content, which compromises the quality of hydration products and weakens interparticle bonding. Additionally, the evaporation of excess water during hydration creates numerous pores within the cementitious matrix, increasing porosity and ultimately reducing compressive strength.

3.3 Characterization and mechanism analysis

3.3.1 XRD analysis of specimen blocks prepared with different tailings dosage

XRD characterization was employed to investigate the mineral phase evolution of the prepared materials. XRD analysis was conducted on cementitious specimens with tailings incorporation rates of 50%, 60%, 70%, 80%, and 90%, and the results are presented in the figure below. As shown in Figure 14, the specimens with different tailings contents exhibited highly similar diffraction patterns, with calcite as the primary crystalline phase, accompanied by substantial quartz and minor amounts of andradite and calcium silicate hydrate (C-S-H). Compared to the 50% tailings specimen, the 90% tailings specimen demonstrated more intense and numerous diffraction peaks for quartz and calcite, indicating a lower degree of hydration in the high tailings content material. This phenomenon is attributed to the limited dissolution of quartz and calcite from iron tailings under alkaline conditions. As the tailings content increases, the corresponding proportions of slag powder and cement decrease, resulting in fewer active components in the

TABLE 7 Reactivity indices of iron tailings at different ball milling times.

No.	Ball milling time/min	3d compressive strength/MPa	28d compressive strength/MPa	Reactivity index/%
Cement-sand ratio	-	12.5	19.7	100
1	0	7.3	8.4	42.6
2	5	8.1	8.7	44.2
3	10	8.7	11.2	56.9
4	15	10.2	21.3	108.1
5	20	8.7	17.3	87.8
6	25	8.5	15.2	77.2
7	30	8.0	10.1	51.3

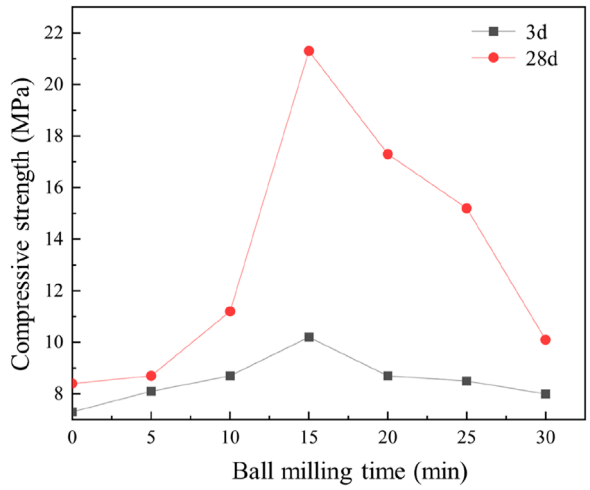

FIGURE 9
Compressive strength of iron tailings-based mortar mixture with different ball milling times.

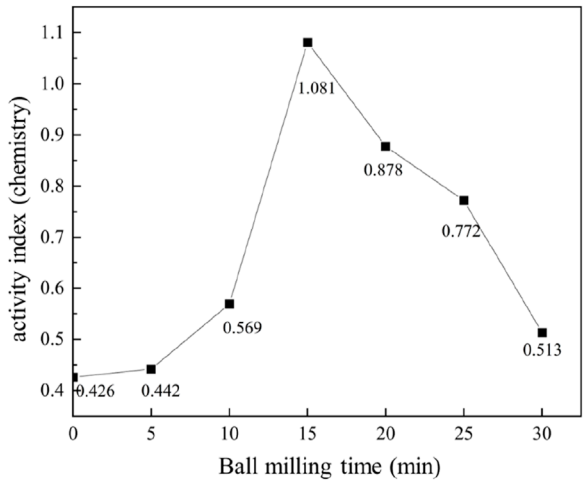

FIGURE 10
Activity index of iron tailings-based mortar mixture at different ball milling times.

cementitious system. Consequently, higher tailings incorporation leads to reduced formation of hydration products.

3.3.2 FTIR analysis of specimen blocks prepared with different tailings dosages

FTIR analysis was performed on test pieces with different tailings dosing, the results illustrated in Figure 15. The FTIR spectrum exhibited characteristic peaks associated with -OH stretching vibrations of water molecules at 3,496 cm^{-1}, 2,512 cm^{-1}, and 1,653 cm^{-1} (Lan et al., 2021f; Sun et al., 2021a). The absorption bands in the ranges of 1,400–1,450 cm^{-1} and 870–890 cm^{-1} were identified as characteristic peaks of calcium silicate hydrate (C-S-H). Specifically, the peaks at 1,425 cm^{-1} and 873 cm^{-1} confirmed the formation of C-S-H gel within the specimens. However, in the 90% tailings sample, these peaks appeared broad and less distinct, indicating a lower concentration of hydration products (Lan et al., 2021c). This reduction in C-S-H formation is attributed to the excessive iron tailings content, which limits the availability of reactive components necessary for hydration. Consequently, the diminished formation of hydration products directly correlates with the observed reduction in compressive strength of the cementitious material.

3.3.3 XRD analysis of specimens prepared at different curing ages

Comparative XRD analysis reveals distinct phase evolution patterns in the cementitious materials versus raw tailings (Figure 16). As demonstrated in the figure above, the cementitious specimens exhibited markedly reduced diffraction intensities compared to the original tailings, signifying partial dissolution of calcite and quartz minerals under alkaline activation, accompanied by the formation of hydration products. At the 3-day

TABLE 8 Orthogonal test results.

Test no.	Slag powder/g	Cement/g	Sodium hydroxide/g	Odium silicate/g	Tailings dosing	Water-cement ratio	Compressive strength/MPa	
							7 d	28 d
1	10	36	8	8	87.2%		2.0	2.5
2	10	44	16	16	85.0%		3.1	4.1
3	10	52	24	24	82.8%		3.0	3.4
4	20	36	16	24	84.4%		2.4	3.5
5	20	44	24	8	82.2%	0.45	3.5	4.8
6	20	52	8	16	80.0%		5.7	6.7
7	30	36	24	16	81.7%		3.5	6.3
8	30	44	8	24	79.4%		4.0	6.9
9	30	52	16	8	77.2%		5.2	6.1

10.3389/fbuil.2025.1672953

10.3389/fbuil.2025.1672953

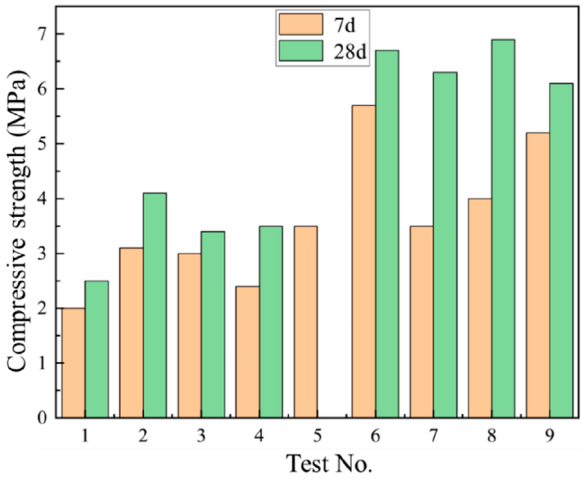

FIGURE 11
Compressive strength of different test groups.

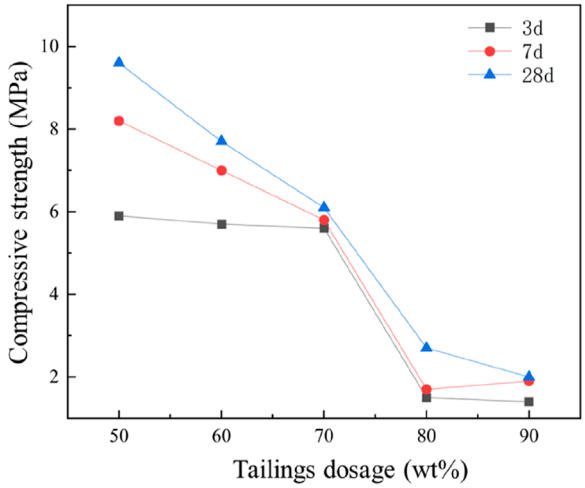

FIGURE 12
Effect of different tailings dosage on the properties of cementitious materials.

TABLE 9 Analysis of orthogonal test results.

Targets		Factor			
		A	B	C	D
7 d-compressive strength/MPa	K1	2.70	2.63	3.9	3.57
	K2	3.87	3.53	3.57	4.10
	K3	4.23	4.63	3.33	3.13
	R	1.53	2	0.57	0.97
		Degree of influence of factors: BADC			
		Optimal combination of factors: $B_3A_3D_2C_1$			
28-compressive strength/MPa	K1	3.33	4.1	5.37	4.47
	K2	5	5.27	4.57	5.7
	K3	6.43	5.4	4.83	4.6
	R	3.1	1.3	0.8	1.23
		Degree of influence of factors: ABDC			
		Optimal combination of factors: $A_3B_3D_2C_1$			

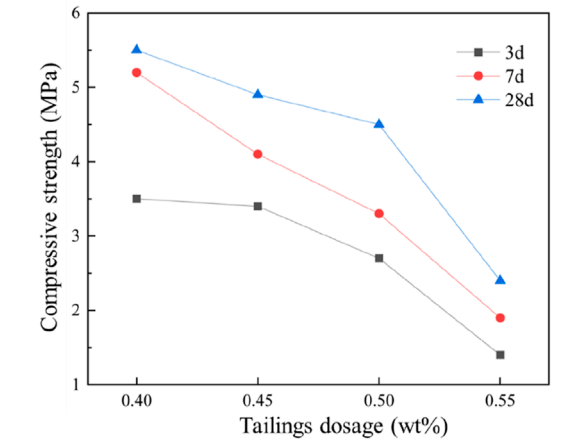

FIGURE 13
Effect of different water cement ratios on the compressive strength of specimens.

curing stage, sharp diffraction peaks resembling those of raw tailings were observed, particularly for quartz (26.6 ° 2θ) and calcite (29.4 ° 2θ), with relative intensities maintaining 85%–92% of the original values. This phenomenon indicates limited hydration activity during the initial curing period, where approximately 60%–70% of mineral phases remained unreacted based on Rietveld quantitative analysis.

Progressive peak attenuation occurred with extended curing, showing 35%–42% intensity reduction at 7 days and 58%–65% reduction at 28 days for major crystalline phases. Notably, the emergence of a diffuse scattering halo between 20 °–40 ° 2θ became increasingly prominent with curing duration, accounting for 22.7%, 38.4%, and 45.6% of total scattering intensity at 3, 7, and 28 days respectively. This amorphous hump corresponds to the formation of calcium silicate hydrate (C-S-H) gels and other nanocrystalline phases (1–5 nm crystallite size), characteristic of alkali-activated cementitious systems. The coexistence of residual crystalline peaks and amorphous signatures suggests an incomplete but progressive hydration process, where dissolution-recrystallization mechanisms compete with geopolymerization reactions (Huang et al., 2025).

10.3389/fbuil.2025.1672953

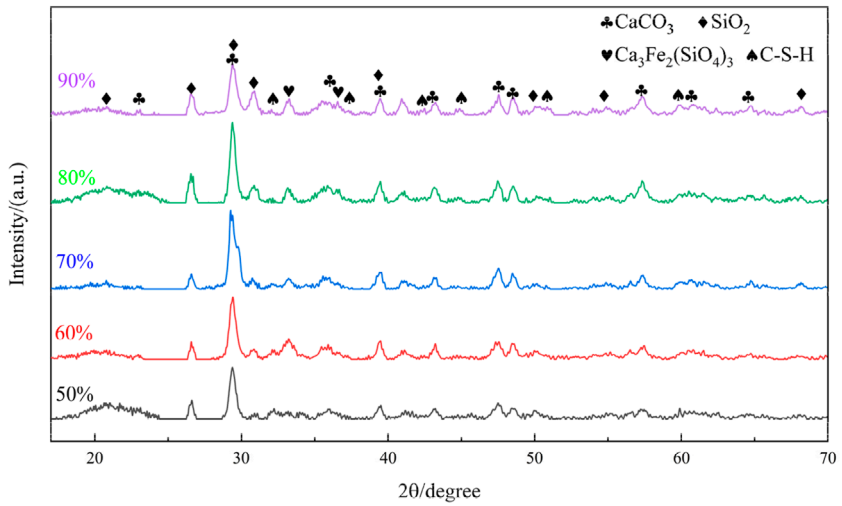

FIGURE 14
XRD plots of test pieces with different tailings dosing.

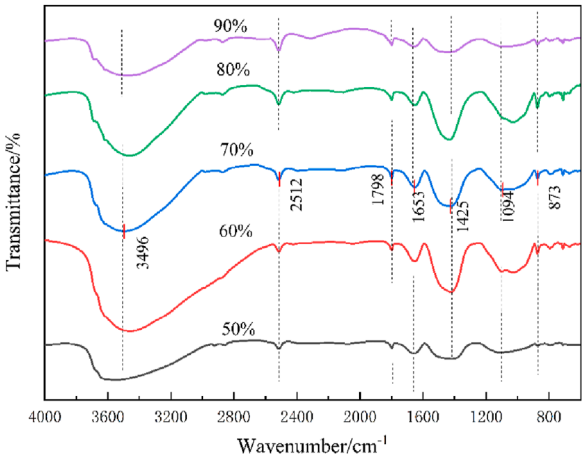

FIGURE 15
FTIR spectra of test pieces with different tailings dosing.

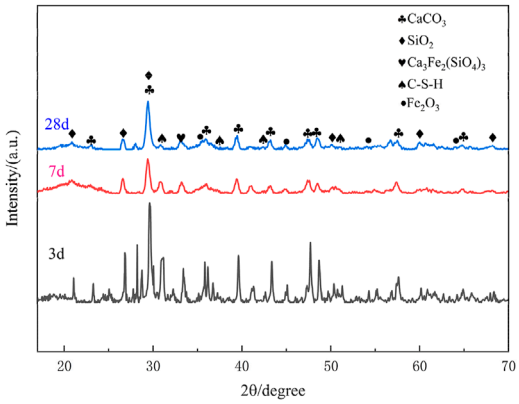

FIGURE 16
XRD plots of specimens at different curing ages.

3.3.4 FTIR analysis of specimens prepared at different curing ages

FTIR analysis was performed on cementitious specimens cured for 3, 7, and 28 days, with the results illustrated in Figure 17. Consistent with prior observations, the spectra across curing ages exhibited similar profiles. A prominent absorption peak at 869 cm^{-1}, attributed to symmetric Si-O stretching vibrations in quartz (Lan et al., 2024), displayed higher intensity at 3 days compared to 7 and 28 days. This observation suggests that during the initial curing stage, the slow dissolution of quartz under alkaline conditions, coupled with the encapsulation of quartz particles by nascent cementitious phases, contributes to the retention of stronger vibrational signatures.

The broad peak near 3,466 cm^{-1}, corresponding to -OH stretching vibrations, arises from structurally bound water and

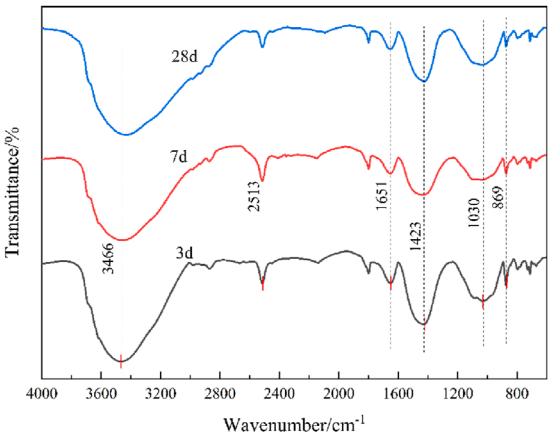

FIGURE 17
Infrared spectra of specimens at different ages of conservation.

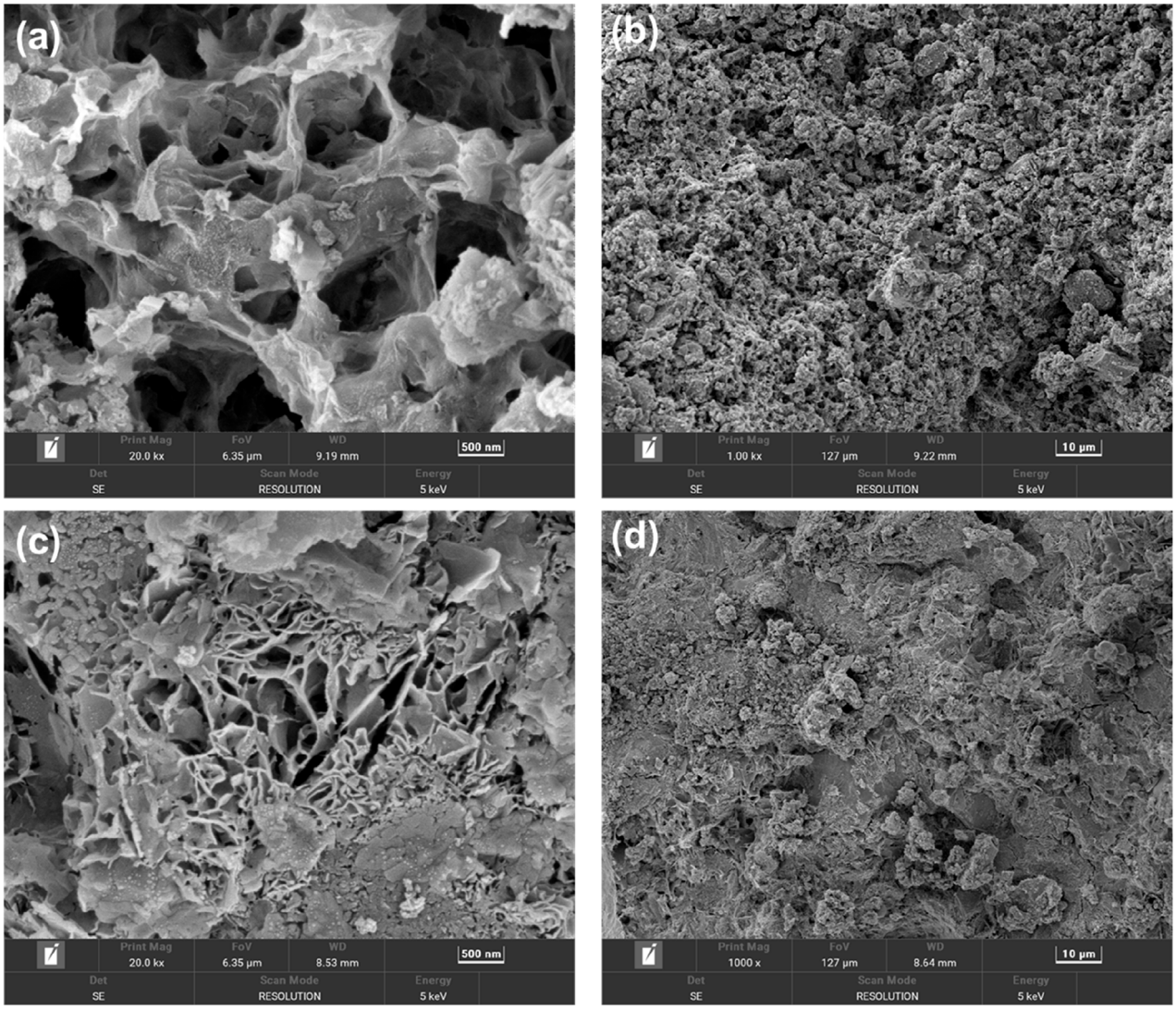

FIGURE 18
SEM analysis of specimens prepared at different curing ages: **(a,b)** 3-day, **(c,d)** 7-day.

asymmetric -OH vibrations in calcium silicate hydrate (C-S-H) (Lan et al., 2020a; Zhang et al., 2025a). Progressive broadening of this peak from 3 to 28 days signifies enhanced C-S-H formation over time. Quantitative deconvolution revealed a 28% increase in peak area for the 3,466 cm^{-1} band between 3 and 28 days, correlating with a 35% rise in bound water content (thermogravimetric analysis). These findings align with hydration kinetics models, where prolonged curing facilitate continuous pozzolanic reactions between active silica/alumina phases and portlandite, yielding additional C-S-H gels.

The attenuated quartz-related peaks and evolving -OH signatures collectively demonstrate the dynamic interplay between mineral dissolution, hydration product formation, and microstructural maturation in alkali-activated systems. This mechanistic understanding is critical for optimizing curing protocols to enhance the performance of tailings-based cementitious materials.

3.3.5 SEM analysis of specimens prepared at different curing ages

As shown in Figure 18a, the presence of large pores within the maintenance age of 3-day material indicates that C-S-H is in the initial formation stage. At the maintenance age of 7 d (Figure 18c), most of the calcite in the crystalline phase have been dissolved, and the spatial network of the C-S-H gel phase has begun to take shape. This corresponds to the XRD results in Section 3.3.3., an incomplete but progressive hydration process with dissolution-recrystallization mechanisms. The generated C-S-H substance is stripped off from the surface of the iron tailings particles and moves towards the liquid phase (Gitari et al., 2018; Lan et al., 2025). Some of them will insert into the gel structure with a spatial network structure; thereby increasing the density of the material. During the continuous development of the hydration process, the crystallization process and the gelation process overlap with each other, and the structural density of the material will increase

accordingly, thereby enhancing the mechanical properties of the material.

3.4 Carbon emission reduction benefits

Substituting cement with iron tailings or similar industrial byproducts significantly reduces carbon emissions. For slag Portland cement—a common iron tailing-blended system—production emits approximately 659 kg CO_2eq per ton, compared to 895 kg CO_2eq for ordinary Portland cement, achieving a 26% reduction (236 kg saved per ton). This stems from lowered clinker requirements and reduced calcination energy. At the concrete scale, mixes incorporating slag powder emit ~231.7 kg CO_2 eq/m^3, roughly 5% lower than conventional concrete (244.1 kg CO_2 eq/m^3), primarily due to cement displacement.

These savings scale substantially in real-world applications. For example, a public housing project in Hong Kong substituting 35% of cement with slag powder cut annual emissions by 3,700 tons of CO_2—equivalent to planting 16,000 trees yearly. Studies confirm such blends also enhance durability, indirectly reducing long-term emissions by extending infrastructure lifespan and minimizing maintenance. While exact figures for tailings-only systems vary, the trend remains clear: even partial cement replacement with mineral wastes delivers measurable, scalable CO_2 reductions aligned with circular economy goals.

4 Conclusion

This study investigated the resource utilization of iron tailings rich in hematite and calcite by employing mechanical activation and alkali activation to enhance tailings reactivity. The prepared cementitious materials incorporated approximately 80% iron tailings combined with cement and slag powder. The effects of ball milling duration and alkali dosage on tailings activity were systematically analyzed, and the optimal mix proportion was determined through orthogonal experiments. Hydration mechanisms were elucidated using XRD and FTIR analyses. The principal conclusions are as follows:

1. Multimodal characterization (XRF, FTIR, XRD) revealed that the iron tailings contained predominant Fe (41.248%), Ca (33.949%), and Si (20.211%), primarily existing as hematite and calcite. Particle size distribution was concentrated within 1–100 μm.
2. Mechanical ball milling effectively refined particle size distribution, with optimal activity index (108.1%) achieved after 15 min of milling. Alkali dosage demonstrated a critical influence on mechanical performance: 6% alkali activator yielded the highest compressive strength (7.9 MPa after 28-day curing). The cementitious material exhibited standard consistency water demand of 42%, initial setting time of 61 min, and final setting time of 107 min, indicating latent hydraulic properties.
3. Orthogonal testing identified slag powder and cement as key performance modifiers. The optimal formulation (30 g slag powder, 52 g cement, 16 g NaOH, and 8 g sodium silicate per 100 g tailings) achieved superior compressive strength. XRD/FTIR analyses demonstrated that higher tailings content reduced cement/slag proportions, thereby limiting dissolution of quartz and calcite in alkaline environments and delaying hydration product formation. Prolonged curing enhanced progressive reactions between active components and alkaline phases, facilitating hydration product development.

4.1 Research limitations and prospects

This work provides fundamental insights into the preparation and hydration mechanisms of iron tailing-based cementitious materials. However, two limitations warrant further investigation:

1. Current activation strategies focused solely on mechanical and chemical methods; future studies should explore chemical-thermal-mechanical composite activation for enhanced tailings reactivity.
2. Microstructural characterization was limited to XRD/FTIR; supplementary techniques (SEM, hydration heat analysis, TGA) could provide comprehensive understanding of hydration kinetics and phase evolution.

These findings advance the sustainable utilization of iron tailings while highlighting critical pathways for optimizing low-carbon cementitious materials in construction applications.

Data availability statement

The original contributions presented in the study are included in the article/supplementary material, further inquiries can be directed to the corresponding authors.

Author contributions

XL: Conceptualization, Data curation, Funding acquisition, Investigation, Software, Validation, Visualization, Writing – original draft, Writing – review and editing. JZ: Data curation, Investigation, Methodology, Software, Validation, Writing – original draft. YZ: Formal Analysis, Supervision, Validation, Visualization, Writing – review and editing. SD: Methodology, Project administration, Resources, Validation, Writing – review and editing. MN: Investigation, Resources, Writing – original draft. SL: Funding acquisition, Project administration, Writing – review and editing.

Funding

The author(s) declare that financial support was received for the research and/or publication of this article. This work was supported by the Natural Science Foundation of Hubei Province (2023AFB269), the National Natural Science Foundation of China (52470160), the Key Research and Development Program of Hubei Province (2024BCB086), and the Research Funding of Wuhan Polytechnic University No. 2024RZ025.

Conflict of interest

The authors declare that the research was conducted in the absence of any commercial or financial relationships that could be construed as a potential conflict of interest.

Generative AI statement

The author(s) declare that no Generative AI was used in the creation of this manuscript.

Any alternative text (alt text) provided alongside figures in this article has been generated by Frontiers with the support of artificial intelligence and reasonable efforts have been made to ensure accuracy, including review by the authors wherever possible. If you identify any issues, please contact us.

Publisher's note

All claims expressed in this article are solely those of the authors and do not necessarily represent those of their affiliated organizations, or those of the publisher, the editors and the reviewers. Any product that may be evaluated in this article, or claim that may be made by its manufacturer, is not guaranteed or endorsed by the publisher.

References

Almeida, V. O., Lima, N., and Schneider, I. A. H. (2023). Simplified hydrometallurgical route for the synthesis of silica-free hematite from iron ore tailings. *Miner. Eng.* 200, 108140. doi:10.1016/j.mineng.2023.108140

Chen, X., Ke, X., Zhao, Z., Wang, D., Duan, J., Du, Y., et al. (2025). Copper slag-aided mechanochemical detoxification soda ash chromite ore processing residue and long-term stabilization: efficient reduction and reoccurrence inhibition of Cr(VI). *J. Clean. Prod.* 488, 144674. doi:10.1016/j.jclepro.2025.144674

Cui, X., Ning, X., Zhang, J., Zhang, D., Qiu, G., and Wang, Y. (2025). Insights into sulfur migration and transformation during the magnetization roasting of iron tailings and textile dyeing sludge. *Waste Manag.* 191, 81–88. doi:10.1016/j.wasman.2024.11.005

Gitari, M. W., Akinyemi, S. A., Thobakgale, R., Ngoejana, P. C., Ramugondo, L., Matidza, M., et al. (2018). Physicochemical and mineralogical characterization of Musina mine copper and New Union gold mine tailings: implications for fabrication of beneficial geopolymeric construction materials. *J. Afr. Earth Sci.* 137 (jan.), 218–228. doi:10.1016/j.jafrearsci.2017.10.016

Gong, L., Liang, J., Kong, L., Chen, B., Li, Y., and Tian, G. (2021). Synthesis of high-performance copper barium silicate composite pigment from waste iron ore tailings. *Ceram. Int.* 47 (19), 27987–27997. doi:10.1016/j.ceramint.2021.06.230

Huang, X., Tu, J., Wang, H., Xue, F., Zhao, X., Xiang, Y., et al. (2025). Activated nickel tailings for remediation of arsenic-contaminated soils: tailings activation, leaching toxicity and passivation mechanisms. *J. Environ. Chem. Eng.* 13 (2), 115912. doi:10.1016/j.jece.2025.115912

Jahanshahi, F. S., and Ghanizadeh, A. R. (2024). Compressive strength, durability, and resilient modulus of cement-treated magnetite and hematite iron ore tailings as pavement material. *Constr. Build. Mater.* 447, 138076. doi:10.1016/j.conbuildmat.2024.138076

Lan, J., Sun, Y., Guo, L., Du, Y., Du, D., Zhang, T. C., et al. (2019a). Highly efficient removal of As(V) with modified electrolytic manganese residues (M-EMRs) as a novel adsorbent. *J. Alloys Compd.* 811, 151973. doi:10.1016/j.jallcom.2019.151973

Lan, J., Sun, Y., Guo, L., Li, Z., Du, D., and Zhang, T. C. (2019b). A novel method to recover ammonia, manganese and sulfate from electrolytic manganese residues by bio-leaching. *J. Clean. Prod.* 223, 499–507. doi:10.1016/j.jclepro.2019.03.098

Lan, J., Sun, Y., Du, Y., Du, D., Zhang, T. C., and Li, J. (2020a). Environmentally-friendly bioleaching of manganese from pyrolusite: performance and mechanisms. *J. Clean. Prod.* 249, 119354. doi:10.1016/j.jclepro.2019.119354

Lan, J., Sun, Y., Huang, P., Du, Y., Zhan, W., Zhang, T. C., et al. (2020b). Using electrolytic manganese residue to prepare novel nanocomposite catalysts for efficient degradation of Azo Dyes in Fenton-like processes. *Chemosphere* 252, 126487. doi:10.1016/j.chemosphere.2020.126487

Lan, J., Dong, Y., Sun, Y., Fen, L., Zhou, M., Hou, H., et al. (2021a). A novel method for solidification/stabilization of Cd(II), Hg(II), Cu(II), and Zn(II) by activated electrolytic manganese slag. *J. Hazard. Mater.* 409, 124933. doi:10.1016/j.jhazmat.2020.124933

Lan, J., Dong, Y., Xiang, Y., Zhang, S., Mei, T., and Hou, H. (2021b). Selective recovery of manganese from electrolytic manganese residue by using water as extractant under mechanochemical ball grinding: mechanism and kinetics. *J. Hazard. Mater.* 415, 125556. doi:10.1016/j.jhazmat.2021.125556

Lan, J., Sun, Y., Chen, X., Zhan, W., Du, Y., Zhang, T. C., et al. (2021c). Bio-leaching of manganese from electrolytic manganese slag by Microbacterium trichothecenolyticum Y1: mechanism and characteristics of microbial metabolites. *Bioresour. Technol.* 319, 124056. doi:10.1016/j.biortech.2020.124056

Lan, J., Sun, Y., Tian, H., Zhan, W., Du, Y., Ye, H., et al. (2021d). Electrolytic manganese residue-based cement for manganese ore pit backfilling: performance and mechanism. *J. Hazard. Mater.* 411, 124941. doi:10.1016/j.jhazmat.2020.124941

Lan, J., Zhang, S., Dong, Y., Li, J., Li, S., Feng, L., et al. (2021e). Stabilization and passivation of multiple heavy metals in soil facilitating by pinecone-based biochar: mechanisms and microbial community evolution. *J. Hazard. Mater.* 420, 126588. doi:10.1016/j.jhazmat.2021.126588

Lan, J., Zhang, S., Mei, T., Dong, Y., and Hou, H. (2021f). Mechanochemical modification of electrolytic manganese residue: ammonium nitrogen recycling, heavy metal solidification, and baking-free brick preparation. *J. Clean. Prod.* 329, 129727. doi:10.1016/j.jclepro.2021.129727

Lan, J., Dong, Y., Kai, M.-F., Hou, H., and Dai, J.-G. (2024). Investigation of waste alkali-activated cementing material using municipal solid waste incineration fly ash and dravite as precursors: mechanisms, performance, and on-site application. *J. Hazard. Mater.* 465, 133416. doi:10.1016/j.jhazmat.2023.133416

Lan, J., Xiang, Y., Zhao, S., Shao, Y., and Hou, H. (2025). *In-situ* cementation backfill of alkali-inspired ultrafine copper tailings: performance and principles. *Green Smart Min. Eng.* 2, 122–132. doi:10.1016/j.gsme.2025.05.002

Li, C., Zhang, X., Yin, Y., Xi, F., Wang, S., Hu, Q., et al. (2025). The mechanism of citric acid and oxalic acid on dissolution of high-silicon iron tailings. *J. Industrial Eng. Chem.* 143, 319–326. doi:10.1016/j.jiec.2024.08.034

Liu, J., An, S., and Zhang, Y. (2023). Mechanism of regulating the mechanical properties and paste structure of supersulfated cement through ultrafine iron tailings powder. *Cem. Concr. Compos.* 140, 105061. doi:10.1016/j.cemconcomp.2023.105061

Närhi, P., Räisänen, M. L., Sutinen, M.-L., and Sutinen, R. (2012). Effect of tailings on wetland vegetation in Rautuvaara, a former iron–copper mining area in northern Finland. *J. Geochem. Explor.* 116-117, 60–65. doi:10.1016/j.gexplo.2012.03.005

Pan, C., Sun, Y., Dong, Y., Hou, H., Kai, M.-F., and Lan, J. (2024a). Efficient carbamazepine degradation by modified copper tailings and PMS system: performance evaluation and mechanism. *J. Hazard. Mater.* 465, 133198. doi:10.1016/j.jhazmat.2023.133198

Pan, C., Wang, Y., Fu, C., and Lan, J. (2024b). Copper slag based catalytic material was prepared using a one-pot method to efficiently activate of peroxymonosulfate for degradation of carbamazepine. *J. Environ. Chem. Eng.* 12 (6), 114631. doi:10.1016/j.jece.2024.114631

Pan, C., Li, Y., Zuo, S., Zhang, D., Dai, G., Liu, S., et al. (2025a). Efficient catalytic degradation of chlorinated volatile organic compounds by porous graphitized carbon supported CuFeS2 via activation of hydrogen peroxide. *Chem. Eng. J.* 509, 161395. doi:10.1016/j.cej.2025.161395

Pan, C., Zhang, Q., Zhang, W., Bao, J., Dai, G., Liu, S., et al. (2025b). Wet scrubbing coupled with advanced oxidation process for removal of chlorobenzene: a study of performance and mechanisms. *Environ. Res.* 268, 120779. doi:10.1016/j.envres.2025.120779

Pramanik, S., Kumari, A., Sahu, S. K., and Munshi, B. (2024). Extraction of metal values from iron-rich mine tailings via chloridized roasting and water leaching. *Waste Manag. Bull.* 2 (2), 113–121. doi:10.1016/j.wmb.2024.04.003

Qin, S., Dou, S., Ma, S., Zhang, Z., Hu, Y., Li, Y., et al. (2024). Enhanced recovery of low-grade copper ore and associated precious metals from iron tailings: a case study in China. *Colloids Surfaces A Physicochem. Eng. Aspects* 699, 134656. doi:10.1016/j.colsurfa.2024.134656

Qiu, G., Ning, X., Zhang, D., Deng, J., and Wang, Y. (2024). The enrichment and transformation mechanism of Pb and Cu in suspension magnetization roasting and magnetic separation from iron tailings. *Waste Manag.* 184, 82–91. doi:10.1016/j.wasman.2024.05.034

Que, Y., Huang, H., Ma, H., Lin, Y., and Jiang, Z. (2024). Enhancing sustainable subgrade engineering using soil tuff for modifying iron tailings sand: a comprehensive

engineering performance and sustainability analysis. *J. Environ. Chem. Eng.* 12 (6), 114585. doi:10.1016/j.jece.2024.114585

Sadeghieh, S. M., Ahmadi, A., and Hosseini, M. R. (2020). Effect of water salinity on the bioleaching of copper, nickel and cobalt from the sulphidic tailing of Golgohar Iron Mine, Iran. *Hydrometallurgy* 198, 105503. doi:10.1016/j.hydromet.2020.105503

Sun, Y., Du, Y., Lan, J., Zhan, W., and Zhang, T. C. (2021a). A new method (ball milling and sodium sulfide) for mechanochemical treatment of soda ash chromite ore processing residue. *J. Hazard. Mater.* 415, 125601. doi:10.1016/j.jhazmat.2021.125601

Sun, Y., Lan, J., Chen, X., Ye, H., Du, D., Li, J., et al. (2021b). High arsenic levels in sediments, Jianghan Plain, central China: vertical distribution and characteristics of arsenic species, dissolved organic matter, and microbial community. *J. Geochem. Explor.* 228, 106822. doi:10.1016/j.gexplo.2021.106822

Sun, Y., Wu, Z., Lan, J., Liu, Y., Du, Y., Ye, H., et al. (2025). Effect of sulfate-reducing bacteria (SRB) and dissimilatory iron-reducing bacteria (DIRB) coexistence on the transport and transformation of arsenic in sediments. *Water Res.* 270, 122834. doi:10.1016/j.watres.2024.122834

Tian, G., Hua, X., Nie, K., Li, Y., Zhang, K., Qu, W., et al. (2024). Lamellar mesoporous Mg-containing silicate adsorbents derived from iron ore tailings for high-efficient adsorption of mycotoxins and antibiotics. *Sep. Purif. Technol.* 330, 125556. doi:10.1016/j.seppur.2023.125556

Wang, H., Gu, X., Xu, X., Liu, J., Zhu, Z., and Wang, S. (2024). The effects of iron tailings on steel slag-based cementitious systems: strength, hydration products, and volume stability. *J. Build. Eng.* 91, 109702. doi:10.1016/j.jobe.2024.109702

Wei, M., Wei, W., Li, Y., Liu, L., Zhong, F., and Xue, Q. (2023). Maximizing the pozzolanic potential of superfine iron tailings for low-carbon stabilization: application of high-calcium geopolymer. *Resour. Conservation Recycl.* 198, 107198. doi:10.1016/j.resconrec.2023.107198

Wei, H., Song, B., Huan, Q., Song, C., Wang, S., and Song, M. (2024). Preparation of iron tailings-based porous ceramsite and its application to lead adsorption: characteristic and mechanism. *Sep. Purif. Technol.* 342, 126839. doi:10.1016/j.seppur.2024.126839

Xiang, Y., Lan, J., Cai, Y., Wang, Y., Dong, Y., and Hou, H. (2023). Preparation of nickel–cobalt tailings-based cementing materials by mechano-chemical activation: performance and mechanism. *Constr. Build. Mater.* 408, 133836. doi:10.1016/j.conbuildmat.2023.133836

Xiang, Y., Lan, J., Cai, Y., Dong, Y., and Hou, H. (2024a). Modified nickel–cobalt tailing activated PMS for highly efficient degradation of organic pollutants: multiple-scale effect and active sites. *Chem. Eng. J.* 482, 149196. doi:10.1016/j.cej.2024.149196

Xiang, Y., Lan, J., Dong, Y., Zhou, M., Hou, H., and Huang, B.-T. (2024b). Pollution control performance of solidified nickel-cobalt tailings on site: bioavailability of heavy metals and microbial response. *J. Hazard. Mater.* 471, 134295. doi:10.1016/j.jhazmat.2024.134295

Yan, Y., Du, X., and Kuang, Y. (2024). Study on the influence of nickel-iron alloy powder on the mechanical strength and electromagnetic shielding effectiveness of iron ore tailings/cement composite. *Case Stud. Constr. Mater.* 21, e03740. doi:10.1016/j.cscm.2024.e03740

Yu, C., Yu, M., Ma, R., Wei, S., Jin, M., Jiao, N., et al. (2024). A novel alteromonas phage with tail fiber containing six potential iron-binding domains. *Microbiol. Spectr.* 13 (1), e00934-24. doi:10.1128/spectrum.00934-24

Zeng, T., Xue, S., Zhuang, S., Zhou, X., Hou, H., Huang, B.-T., et al. (2025). Activated electrolytic manganese residue-based environmental materials for mine remediation: performance and mechanism. *J. Hazard. Mater.* 482, 136560. doi:10.1016/j.jhazmat.2024.136560

Zhang, S., Lan, J., Yu, L., Luo, Y., Zeng, T., Zhou, M., et al. (2025a). Preparation of multi-defect calcite based environmental materials from high-alumina fly ash: mechanism of performance enhancement for Pb removal. *J. Environ. Chem. Eng.* 13 (2), 115539. doi:10.1016/j.jece.2025.115539

Zhang, S., Yu, L., Lv, Y., Zeng, T., Hou, H., and Lan, J. (2025b). High efficiency selective recovery of Al from high-alumina fly ash by multistage activation and carbonation on-site application scale. *Chem. Eng. J.* 506, 160003. doi:10.1016/j.cej.2025.160003

Zhao, B., Wang, G., Wu, B., and Kong, X. (2023). A study on mechanical properties and permeability of steam-cured mortar with iron-copper tailings. *Constr. Build. Mater.* 383, 131372. doi:10.1016/j.conbuildmat.2023.131372